RAPID DYNAMIC LOAD ESTIMATION PROCEDURE FOR LIFTING PROPELLERS IN FORWARD FLIGHT

Felix Möhren[1], Ole Bergmann[1], Frank Janser[1], Carsten Braun[1], Kai-Uwe Schröder[2]
[1]FH Aachen, Faculty of Aerospace Engineering, Aachen, Germany
[2]RWTH Aachen University, Institute of Structural Mechanics and Lightweight Design, Aachen, Germany

Abstract

Lifting propellers operate at oblique inflow and thus encounter severe dynamic loads during forward flight, impacting structural integrity, fatigue, and vibration. Numerical optimisation approaches consider aerodynamic, structural mechanical, and aeroacoustic aspects within preliminary design. To also account for dynamic loads during forward flight, a novel procedure allows their rapid estimation. Based on steady-state simulations combining strip theory and beam finite elements, aerodynamic excitation, damping, and stiffness are defined in the frequency domain. Loads are derived through a linear inflow model and quasi-steady aerodynamics. Damping and stiffness loads are linearised and transferred into matrix form to calculate the frequency response. The computationally expensive need for simulations in the time domain is thus avoided. Applicability extends to both fixed and variable pitch lifting propellers utilised in large multicopters for cargo or passenger transportation. Comparisons to time-marching simulations show good agreement with deviations of approximately 10%. The analytical derivation yields physical insights to understand and reduce dynamic loads and their magnification due to resonance.

1 NOTATION

Latin Symbols

$A = \alpha_A$	Crosswind angle, deg
$\boldsymbol{C_R}, \boldsymbol{C_{AE}}$	Rayleigh and aerodynamic damping matrix
C_μ	Lift deficiency function
c_l	Lift coefficient
$c_{l,\alpha}$	Lift curve slope, 1/rad
e_x, e_y, e_z	Elemental coordinate system
i	Integer index value
j	$\sqrt{-1}$
$\boldsymbol{F_{AE,std}}, \boldsymbol{F_{CF}}$	Steady aerodynamic and centrifugal loads vector
$\boldsymbol{F_{std}}, \boldsymbol{F_{dyn}}$	Steady and dynamic loads vector
$\dot{h}$	Plunge velocity, m/s
$\boldsymbol{K_L}, \boldsymbol{K_G}, \boldsymbol{K_{SP}}$	Linear, geometric, and spin-softening matrix
L	Lift
$\boldsymbol{M}$	Mass matrix
p	Distributed load, N/m
q	Dynamic pressure, Pa
r, R	Dimensionless and dimensional blade radius, -, m
t	Time, s
$\boldsymbol{u}$	Nodal deformations vector
v	Velocity, m/s
w	Sectional air velocity, m/s
x_H, y_H, z_H	Helicopter coordinate system
x_P, y_P, z_P	Propeller-fixed coordinate system

Greek Symbols

$\alpha, \dot{\alpha}$	Angle of attack and its time derivative, deg and deg/s
α_z	Zero lift angle of attack, deg
$\Theta, \Theta_{x,y,z}$	Built-in and elastic twist angle, deg
λ	Inflow ratio
μ	Helicopter advance ratio

ξ	Non-dimensional beam coordinate
ρ	Air density, kg/m^3
Φ	Inflow angle of attack, deg
X	Wake skew angle, deg
Ψ	Propeller azimuthal position, deg
ω	Excitation frequency, rad/s
Ω	Propeller rotational speed, rad/s

Subscripts

A	Aircraft
AE	Aero
CF	Centrifugal
dyn	Dynamic
ext	External
H	Helicopter
i	Induced
lin	Linearised
NI	Non-uniform inflow
P	Perpendicular
QS	Quasi-steady
R	Radial
std	Steady
SD	Structural dynamic
T	Tangential
0	Values of steady simulation
∞	Aircraft flight velocity

Acronyms

MDO	Multidisciplinary Optimization
EF	Excitation Factor
DEF	Dynamic Excitation Factor

2 INTRODUCTION

Propeller-based propulsion systems have been investigated to a large extent in recent times since they offer high propulsive efficiency. The design of propellers necessitates a comprehensive consideration of aerodynamics, structural mechanics, and aeroacoustics [1, 2]. All three disciplines are coupled since each blade is an elastic beam [3, 4]. Due to interdisciplinarity, multiple research groups focus on multidisciplinary optimisation approaches (MDO) [5–7].

Novel air taxis and cargo drones employ propellers to generate lift during forward flight. These propulsors have a structural layout and blade root like a conventional propeller. Still, they are operated like a helicopter rotor without a swashplate, i.e., they are fixed pitch or incorporate only a collective pitch adjustment. Due to these peculiarities, they are referred to as lifting propellers. The blades encounter severe transverse flow. Since the pitch cannot be adjusted selectively, transverse inflow limits the operational capabilities of lifting propellers to 100-150km/h. Transverse flow leads to oscillating angles of attack and inflow velocities within each revolution, resulting in dynamic loads. Experimental tests unveiled severe vibrations of lifting propellers during operation, impacting aerodynamic performance, structural integrity, and passenger comfort.

While propeller optimisation primarily centres on aerodynamics and aeroacoustics, structural integrity is commonly considered as a constraint [8, 9]. However, structural deformations significantly impact aerodynamic performance. Complex swept or coned planforms might be implemented to achieve advantages regarding performance and noise emissions [10], introducing further couplings [11]. Consequently, design and optimisation schemes must determine aeroelastic performance and ensure structural integrity during operational life.

Static strength is the most apparent structural constraint, as included in many frameworks, but is not exhaustive. Unfortunately, some research groups solely implemented static strength requirements in their routines [8, 9, 12]. Fatigue, frequency response, and aeroelastic instabilities are also mandatory for a vital design [13–15], even though not all of them can be estimated by reduced order methods.
Structural Eigenmode analysis rapidly determines natural blade frequencies and safety margins to excitation frequencies during operation [16]. Unfortunately, aerodynamic loads vary Eigenmodes and primarily dictate the dynamic magnification in the vicinity of resonance frequencies due to aerodynamic damping, as will be shown in this paper. Coupled models are consequently crucial to determine dynamic loads. Those loads are necessary to validate dynamic strength and evaluate vibratory shaft loads. Coupled aeroelastic simulations can determine these loads in the time domain at a significant computational cost [17].

Research in the helicopter industry has included aeroelastic tailoring, frequency placement and stability margins in MDO schemes for decades [18, 19]. Friedmann presents a comprehensive review [20]. He also reviews aeroelasticity with particular application to prop-rotors of VTOL vehicles like the X-15 [21]. In recent research, coupled aeroelastic rotor considerations combine beam theories with unsteady aerodynamics in the time domain. Beam theories and one-dimensional coupling schemes require very low computational costs. Unsteady aerodynamic theories significantly affect the computational cost since the impact of the wake on aerodynamic forces has to be resolved. Dynamic inflow models developed by Peters and his colleagues efficiently provide the wake feedback on the induced inflow without the need to resolve the wake [22, 23]. Still, these approaches require significantly more time than steady-state simulations.

To the author's knowledge, there is only one estimation procedure published to determine dynamic propeller loads without the need for coupled aeroelastic simulations in the time domain [24]. This approach compares the undisturbed steady-state equilibrium at axisymmetric inflow with a second, disturbed equilibrium condition. It is specifically tailored for General Aviation propellers at small crosswind angles below ten degrees. The next chapter briefly presents the method and its limitations. Unfortunately, the authors showed in a previous investigation that the existing approach is unsuited to estimating dynamic loads of lifting propellers during forward flight, even at low crosswind angles [25].

This paper presents a novel estimation procedure for dynamic loads of lifting propellers during forward flight. The approach encompasses a description of the aerodynamic loads and the subsequent structural response in the frequency domain. Building upon the equations employed in a steady-state simulation, the method provides loads at minimum computational cost. It is important to note that the method relies on various approximations and is not intended to replace more sophisticated simulation approaches in the time domain. Instead, its primary objective is to provide prompt and physics-based estimations for preliminary design purposes or as a constraint in MDO.

3 DYNAMIC PROPELLER LOADS

3.1 Causes of Dynamic Loads

Conventional propellers are primarily operated at steady horizontal flight, i.e., the flight direction is approximately aligned with the rotational axis of the propeller, leading to an axisymmetric inflow into the propeller disk. Since the velocity and mass of the aircraft vary during the flight mission, the overall aircraft angle of attack also varies, leading to a misalignment or crosswind angle. Flight manoeuvres or gust encounters have a similar effect. The misalignment is characterised by a crosswind angle α_A or A and a crosswind component $v_\infty \cdot \sin\alpha_A$, see Figure 1. The crosswind component results in oscillating tangential velocities and angles of attack. In literature, dynamic propeller loads due to inclined inflow are referred to as Aq, Ψq, or 1xP loads (since they have the same angular frequency as the propeller rotational speed Ω and are approximately proportional to the crosswind angle A and the dynamic pressure q). Besides the firing frequency of piston engines and manoeuvre loads, Aq loads are the primary cause of dynamic propeller loads and fatigue [24].

Higher-order oscillations, so-called nxP loads, can occur due to interference with wings, fuselage, or pylon/strut. nxP loads are small and negligible on conventional aircraft as long as they are not in the range of natural blade frequencies.

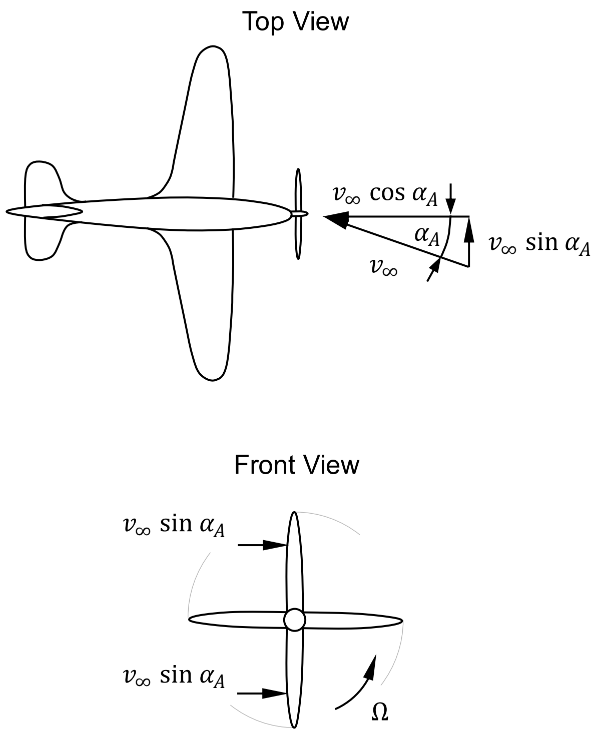

Figure 1: Velocity components at the propeller disk during crosswind encounter

With $A = \alpha_A$ as the crosswind angle, 1xP loads are proportional to the Aq factor, defined as:

$$Aq = A\,\frac{\rho}{2}\,v_\infty^2 \tag{1}$$

For typical propeller applications, the crosswind component $v_\infty \sin\alpha_A$ is significantly smaller than the aircraft's flight velocity, resulting in small crosswind angles α_A. Consequently, small angle assumptions are valid. Since the mass flow is high due to the flight speed, the axial induced velocity v_i is small compared to aircraft flight speed.

3.2 Existing Estimation Procedure

The approach of Amatt et al. [24] assumes that 1xP loads and resulting deformations are both quasi-steady. Dynamic loads and deformations within each rotation are characterised by separate equilibrium states. The first state is the undisturbed flight, i.e., no crosswind component occurs. A second disturbed pseudo steady-state determines loads and deformations at the azimuthal position with maximum Aq value. The variations in loads and deformations quantify the dynamic amplitudes. Aeroelastic interactions are limited to steady torsional deformations, which are iteratively considered. The inflow condition is known a-priori and described with the Aq- or excitation-factor EF, which can be related to each other. Procedures for determining the excitation factor are presented in Ref. [26]. Dynamic strength can be checked in the next step, e.g., by using Goodman diagrams.

The underlying assumptions of this approach are:

- Dynamic loads are approximately a harmonic oscillation with mean values described by the undisturbed steady-state analysis and the amplitudes determined by the differences to a second pseudo steady-state analysis
- Aerodynamic loads and deformations are both quasi-steady
- Aerodynamic damping and inertia loads are negligible
- Amplitude magnification due to excitation in the vicinity of resonances is not considered or generally avoided by fixed safety margins
- Crosswind angles are small, i.e., small angle assumptions are valid

It is worth mentioning that the referred procedure includes strip theory and beam analysis in the original publication. However, Hamilton Standard validated the structural design of the Advanced Turbo Prop [27] (later resulting in the PW-Allison 578-DX [28]) with a similar approach but using finite shell elements instead of beam theory. The approach to estimating the dynamic loads with two separate steady analyses is not limited to specific structural models. Regarding the aerodynamic load calculation, the method inherently requires strip analysis.

4 NOVEL ESTIMATION PROCEDURE

Lifting propellers and helicopter rotors operate at oblique inflow, characterised by the rotor disk angle α_H (subscript H for helicopter) as shown in Figure 2.

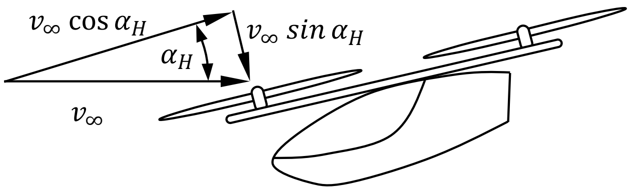

Figure 2: Velocity components into propeller disk during forward flight

Rotor disk angle and propeller crosswind angle are related by

$$\alpha_H = 90° - \alpha_A \tag{2}$$

Due to flight speeds lower than those of fixed-wing aircraft, the mass flow through the propeller disk is comparatively low, requiring high axial induced velocities. The authors previously published a modification of Amatt's approach to include the axial induced velocity in the definition of the Aq factor [25]. Even though including induced velocities reduces the errors of the modified estimation procedure, the approach is still restricted to small crosswind angles, limiting its practical applicability. It is also evident that the neglect of inertia, aerodynamic damping, and amplitude magnification significantly impacts the method's accuracy for flexible blades (lifting propellers commonly have a low disk loading, i.e., a high aspect ratio to reduce power consumption in hover). Including large angles does not impact computational cost, but determining and considering aerodynamic damping and inertia loads in the time domain is expensive within preliminary design or optimization routines.

The novel approach consists of a frequency response analysis with linearised aerodynamic damping, stiffness, and excitation forces. Like the original procedure, strip theory (blade element momentum theory) determines quasi-steady aerodynamic loads. Structural deformations, as determined by a finite beam element analysis incorporating moderate deflections theory, are transferred into an angle of attack variation at each aerodynamic section. 1xP loads and corresponding deformations occur within the first propeller rotational frequency. The impact of higher-order oscillations will be discussed.

Applicability and Constraints

The novel estimation procedure is applicable to lifting propellers without swashplate. Typical applications are large multicopter for urban air mobility and cargo transport or lift + cruise configurations utilizing lifting propellers to take off vertically and accelerate into fixed-wing flight mode. The advance ratio is limited to $\mu \leq 0.3$. Dynamic stall and compressibility effects are neglected (except the Mach correction within XFOIL) since lifting propellers operate at low flight speeds.

4.1 Steady-State Analysis

Prior to the frequency response analysis, a steady-state simulation determines the undisturbed steady equilibrium, i.e., a fictive operational condition with axisymmetric inflow. The resulting matrices and coefficients are required for the linearization of the quasi-steady loads and deformations within the frequency response analysis.

Aerodynamic loads are determined with blade element theory. Even though nonlinear inflow models are available at no computational cost, a uniform induced inflow model determines axial induced velocities to be later directly applicable to the harmonic load calculation, see Eq. (28). XFOIL determines the two-dimensional aerodynamic coefficients for varying Mach and Reynolds numbers within the preprocessor, including steady compressibility corrections and a transition model [29]. Prandtl's tip and root loss correction attenuate the lift distribution [30]. The second author presents a detailed explanation and validation cases in reference [31].

Piecewise straight beam elements connecting the sectional shear centres represent the blade planform of arbitrary shape, as shown in Figure 3. Nonlinear finite elements formulated according to moderate deflection theory iteratively determine the deformations using geometric and spin-softening matrices:

$$\begin{aligned}\boldsymbol{K_{std}}\,\boldsymbol{u_{std}} &= \boldsymbol{F_{std}} = \\ \left(\boldsymbol{K_L} + \boldsymbol{K_G}(\boldsymbol{u}) + \boldsymbol{K_{SP}}(\Omega)\right)\boldsymbol{u_{std}} &= \\ &\boldsymbol{F_{CF}}(\Omega) + \boldsymbol{F_{AE,std}}(\boldsymbol{u})\end{aligned} \tag{3}$$

With $\boldsymbol{K_{std}}$ as the steady stiffness matrix, incorporating the linear, geometric, and spin-softening matrices $\boldsymbol{K_L}, \boldsymbol{K_G}(\boldsymbol{u})$, and $\boldsymbol{K_{SP}}(\Omega)$. The steady external forces $\boldsymbol{F_{std}}$ include the centrifugal loads $\boldsymbol{F_{CF}}(\Omega)$ and the steady aerodynamic loads $\boldsymbol{F_{AE,std}}(\boldsymbol{u})$. $\boldsymbol{u}$ is the nodal deformations vector in the propeller-fixed coordinate system x_P, y_P, z_P. The authors present a more detailed explanation including validation in reference [11]. The aerodynamic loads, as determined at different sections, are interpolated with splines. Orthogonal projections transfer the loads to the structural mesh.

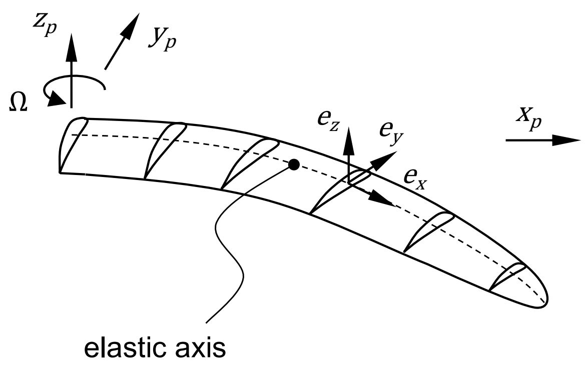

Figure 3: Propeller blade and elemental coordinate system

4.2 Frequency Response Analysis

Due to oblique inflow, structural deformations and aerodynamic loads are oscillating. Since some aerodynamic loads are proportional to deformations and deformation velocities, they are considered as aerodynamic stiffness and damping. Aerodynamic inertia terms are neglected in this quasi-steady approach. Referring to the steady reference point, the governing equation in the time domain is

$$\begin{aligned}\boldsymbol{M}\,\ddot{\boldsymbol{u}} + \boldsymbol{C}\,\dot{\boldsymbol{u}} + \boldsymbol{K}\,\boldsymbol{u} &= \boldsymbol{F} = \\ \boldsymbol{M}\,\ddot{\boldsymbol{u}} + (\boldsymbol{C_R} + \boldsymbol{C_{AE}})\,\dot{\boldsymbol{u}} + (\boldsymbol{K_{std}} + \boldsymbol{K_{AE}})\,\boldsymbol{u} &= \\ &\boldsymbol{F_{std}} + \boldsymbol{F_{dyn}}\end{aligned} \tag{4}$$

With $\boldsymbol{M}$ as the mass matrix, $\boldsymbol{C}, \boldsymbol{C_R}, \boldsymbol{C_{AE}}$ as the total, Rayleigh, and aerodynamic damping matrix, $\boldsymbol{K}$ and $\boldsymbol{K_{AE}}$ as the total and aerodynamic stiffness matrix, and $\boldsymbol{F}$ and $\boldsymbol{F_{dyn}}$ as the total and dynamic force vector. The actual deformations can be decomposed into a steady and dynamic part:

$$\boldsymbol{u} = \boldsymbol{u_{std}} + \boldsymbol{u_{dyn}} \tag{5}$$

Definitions of the steady matrices are in reference [11]. The aerodynamic matrices and load vector will be derived in the following. The non-stationary (quasi-steady) aerodynamic loads are a function of:

$$F_{dyn} = f(\alpha, \dot{\alpha}, \dot{h}, w) \tag{6}$$

With $\alpha, \dot{\alpha}, \dot{h},$ and w as sectional angle of attack, it's time derivative, plunge velocity normal to the incoming air, and sectional air velocity. The quasi-steady aerodynamic loads include damping, stiffening (softening) and external terms, i.e., loads independent of structural deformations.

As shown by others, the external aerodynamic excitation is of harmonic form with excitation frequencies of integer multiples of the rotational speed [32]. Higher-order loads (nxP-loads) are excited but the predominant contribution to the overall loads stems from 1xP loads. The structural response is described by:

$$\boldsymbol{u}_{dyn} = \underline{\hat{\boldsymbol{u}}}_{dyn}\, e^{j\omega t},\ \dot{\boldsymbol{u}} = j\omega\, \underline{\hat{\boldsymbol{u}}}_{dyn}\, e^{j\omega t}, \text{ and } \ddot{\boldsymbol{u}} = -\omega^2\, \underline{\hat{\boldsymbol{u}}}_{dyn}\, e^{j\omega t}, \tag{7}$$

With $\underline{\hat{\boldsymbol{u}}}$ denoting complex amplitudes and

$$\omega = i\Omega,\ \ \mathrm{i} = 1,2,3\ ... \tag{8}$$

ω is the excitation frequency. Subtracting eq. (3) from (4) and inserting (7) yields the dynamic stiffness matrix in the frequency domain:

$$\begin{aligned}(-\omega^2 \boldsymbol{M} + j\omega(\boldsymbol{C_{AE}} + \boldsymbol{C_R}) \\ + (\boldsymbol{K_{AE}} + \boldsymbol{K_{std}}))\ \underline{\hat{\boldsymbol{u}}}_{dyn}\, e^{j\omega t} = \\ \underline{\boldsymbol{K}}_{dyn}\, \underline{\hat{\boldsymbol{u}}}_{dyn}\, e^{j\omega t} = \underline{\hat{\boldsymbol{F}}}_{dyn}\, e^{j\omega t}\end{aligned} \tag{9}$$

The steady stiffness matrix is assumed to be constant. Structural deformations $\boldsymbol{u}$ include translational deformations $u_{x,y,z}$ and rotational deformations $\theta_{x,y,z}$. The torsional deformations equal the angle of attack variation due to structural deformations for straight blades ($\theta_x \approx \alpha_{SD}$). Swept or preconed planforms require a coordinate transformation between the structural and the aerodynamic coordinate system. The inversion of the dynamic stiffness matrix yields the transfer function to determine the structural response

$$\underline{\hat{\boldsymbol{u}}}_{dyn} = \underline{\boldsymbol{H}}(\omega)\, \underline{\hat{\boldsymbol{F}}}_{dyn} \ \text{ with } \ \underline{\boldsymbol{H}}(\omega) = \underline{\boldsymbol{K}}_{dyn}^{-1} \tag{10}$$

4.3 Quasi-Steady Aerodynamic Loads

The derivation of linearised aerodynamic loads requires geometric information on the sectional velocity components. Those are derived for a straight blade but the method can be easily extended to arbitrary planform via the transformation of aerodynamic and structural mechanical degrees of freedom.

Preliminaries

During forward flight, tangential, radial, and axial velocities vary due to an oblique inflow as well as the non-uniform induced velocity field. $\Psi = \Omega t$ describes the azimuthal position of the propeller in its rotational plane, v_T and v_R are the tangential and radial velocity components, respectively, see Figure 4. The axial or perpendicular velocity component v_P is not illustrated.

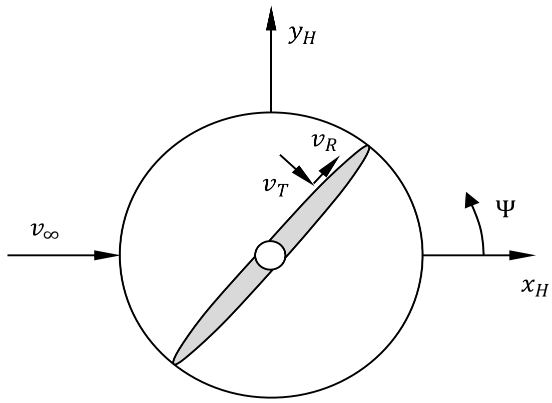

Figure 4: Helicopter coordinate system x_H, y_H

The aerodynamic sectional lift is

$$\frac{dL}{dR} = \frac{\rho}{2} w_0^2 c\, c_l \tag{11}$$

With L as the lift, R as radius, ρ as air density, w_0 as air velocity, c as chord length, and c_l as the lift coefficient. The aerodynamic angle of attack is

$$\alpha = \Theta - \alpha_z - \Phi + \alpha_{SD} \tag{12}$$

With Θ as the initial (built in) twist angle, α_z as the zero-lift angle of attack (usually denoted as α_0 in literature), Φ as the inflow angle of attack, and α_{SD} as the structural torsional deformation, see Figure 5. The subscript 0 indicates the values of the steady simulation. ΩR is the tip speed, r is the dimensionless radius, and $v_{i,T}$ and $v_{i,P}$ are the tangential and perpendicular induced velocities.

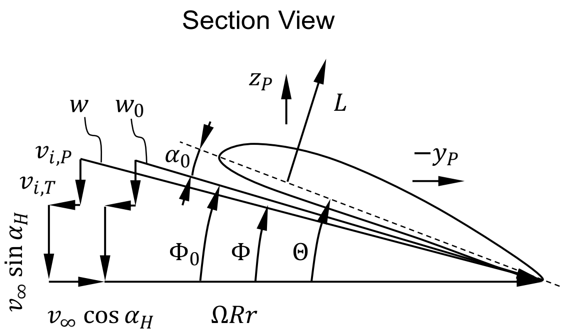

Figure 5: Cross-sectional velocities and angles

The linearised dynamic lift for small perturbations is

$$\left(\frac{dL}{dR}\right)_{dyn} \approx \frac{\partial(dL/dR)}{\partial w}\Delta w + \frac{\partial(dL/dR)}{\partial \alpha}\Delta\alpha = \rho\, w_0\, c\, c_{l0}\, \Delta w + \frac{\rho}{2} w_0^2 c\, c_{l,\alpha,lin}\, \Delta\alpha \tag{13}$$

with the linearised lift curve slope $c_{l,\alpha,lin}$. The impact on drag is neglected since thrust and power consumption primarily depend on the lift. The quadratic variation of wind speed in the first term of Eq. (13) is below 10% and is therefore also neglected. For higher advance ratios, a Taylor-series could be used to include the quadratic variation and increase accuracy, but higher advance ratios are generally unfeasible with fixed pitch blades due to stall.

The dynamic pressure q and the lift are proportional to the square of the wind speed. Accordingly, a harmonic oscillation in wind speed results in 1xP and 2xP variations in lift. The helicopter advance ratio is

$$\mu = \frac{v_\infty \cos(\alpha_H)}{\Omega R} \tag{14}$$

Depending on the rotational speed, flight speeds of 30m/s usually result in an advance ratio μ of below 0.15, yielding velocity variations of below 0.2 at 75% of the radius. As shown in Figure 6, the harmonic variation of wind speed results in 2xP oscillations of the dynamic pressure q, but those amplitudes are negligible at low advance ratios compared to the 1xP contribution.

The aerodynamic loads are unsteady since velocities and inflow angles are time-dependent, resulting in amplitude attenuation and phasing. The reduced frequency of rotary wing section is approximately

$$k = \frac{\omega b}{2w} \approx \frac{\Omega b}{2\Omega Rr} = \frac{1}{2}\frac{b}{Rr} \tag{15}$$

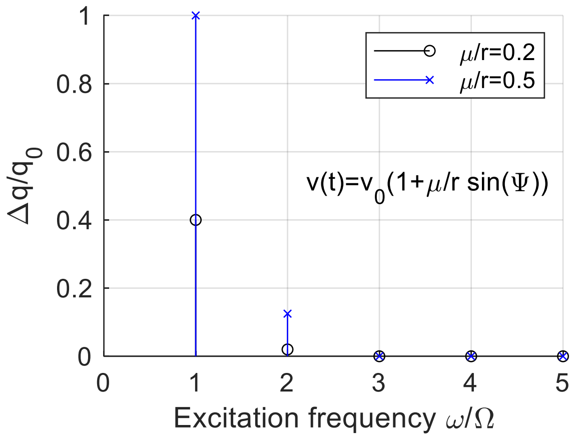

Figure 6: Amplitude spectrum of the dynamic pressure due to time-varying inflow velocity $v(t)$

Since the flow velocity $w = v(t)$ is also time-dependent, the reduced frequency is somewhat ambiguous. Ref. [33] presents and compares different unsteady theories on that topic, both in the time and frequency domain. Johnson further derives a lift attenuation function $C_\mu = f(\Psi)$ in Ref. [32], ch. 10-4, for time-varying inflow velocities. He states that for $\mu/r < 0.7$ and small aspect ratios b/R, the deficiency function C_μ can be approximated by the Theodorsen function. Figure 7 validates this statement for a typical lifting propeller at the 75% Radius section.

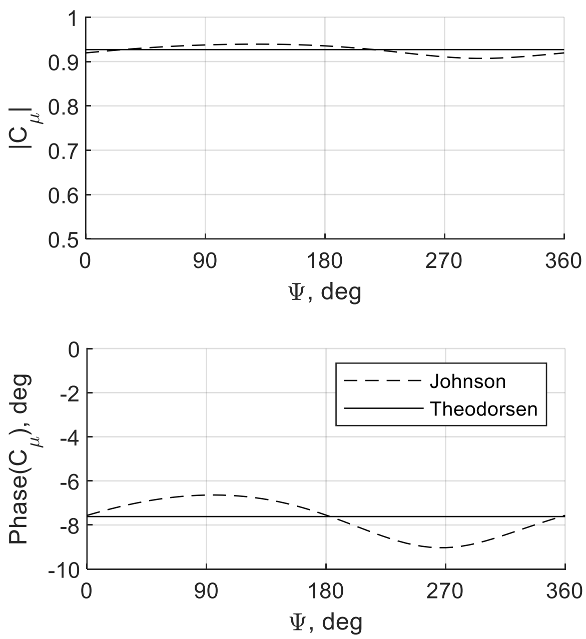

Figure 7: Variation of the aerodynamic attenuation function C_μ for 1xP harmonics during one revolution $\mu/r = 0.2,\ b/R = 1/30,\ \omega = \Omega$

The diagram illustrates two results:

- The Theodorsen function is a proper approximation for the lift attenuation of lifting propellers at low advance ratios
- The lift attenuation is below 10% due to the low reduced frequencies, i.e., the quasi-steady aerodynamics are a reasonable approximation

Since the zero lift angle of attack α_0 and built-in twist angle Θ are constant, the variation in the effective angle of attack is

(16) $$\Delta\alpha = \Delta\alpha_{SD} + \Delta\alpha_{AE} = \Delta\alpha_{SD} + \Delta\alpha_{AE,QS} + \Delta\alpha_{AE,NI}$$

The aerodynamic angle of attack variation $\Delta\alpha_{AE}$ can be differentiated into the quasi-steady angle of attack variation $\Delta\alpha_{AE,QS}$ and the variation $\Delta\alpha_{AE,NI}$ due to the non-uniform inflow angle Φ. Note that

(17) $$\partial\alpha/\partial\Phi = -1, \text{i.e.}, \Delta\alpha_{AE,NI} = -\Delta\Phi$$

Quasi-Steady Angle of Attack Variation $\Delta\alpha_{QS}$

According to quasi-steady thin airfoil theory, the pitch and plunge motion at a radial section result in a variation in effective angle of attack and moment coefficient at the quarter chord length:

(18) $$\Delta\alpha_{QS} = \left(\frac{\dot{h}}{w_0} + \frac{c}{2}\left(\frac{1}{2} - a\right)\frac{\dot{\alpha}}{w_0}\right)$$ $$\mathrm{c}_{\mathrm{m}_{0.25}} = -\frac{\pi}{4}\frac{\dot{\alpha}c}{2w_0}$$

The non-dimensional shear centre position a is the distance between the airfoil mid-chord to the shear centre divided by half of the chord length, positive if the shear centre is closer to the trailing edge. With $\dot{u}$ denoting the structural deformation velocities, the approximation of the plunge velocity is (positive in downward direction)

(19) $$\dot{h} \approx -\dot{u}_z\cos(\Phi_0) + \dot{u}_y\sin(\Phi_0) + \beta\mu\Omega R\cos\Psi$$ With $\beta \approx \frac{du_z}{dx}$

β is the blade flapping angle due to elastic deformations. For preconed propellers, β further includes a constant part.

Like all deformations, the flapping angle consists of a steady and a dynamic amplitude:

(20) $$\beta = \beta_0 + \beta_{dyn}$$

Since β_{dyn} and the perpendicular inflow part of μ are both oscillating at the rotational frequency (1xP), the dynamic contribution β_{dyn} yields a 2xP excitation:

(21) $$\beta_{dyn}(t)\mu\Omega R\cos\Psi = \underline{\hat{\beta}}_{dyn}e^{j\Omega t}\mu\Omega R e^{j\Omega R} = \underline{\hat{\beta}}_{dyn}\mu\Omega R e^{j2\Omega t}$$

To linearise the system, the dynamic part of the flapping angle β_{dyn} is neglected and $\beta \approx \beta_0$. As will be shown by comparisons to transient simulations, the neglection is appropriate for lifting propellers due to the limited dynamic magnification at 2xP.

$\dot{\alpha}$ of Eq. (18) includes structural deformation velocities $\dot{\alpha}_{SD}$ and harmonic angle of attack oscillations $\dot{\alpha}_{AE,NI}$ due to non-uniform inflow conditions:

(22) $$\dot{\alpha} = \dot{\alpha}_{SD} + \dot{\alpha}_{AE,NI}$$

As mentioned above, the torsional deformations in the radial direction directly vary the aerodynamic angle of attack solely for straight blades. Torsional deformations and the blade flapping angle β require coordinate transformation for swept planforms.

Wind Angle Variation ΔΦ

The following calculations assume a rigid blade. The impact of elastic pitch and plunge motion is already considered in $\Delta\alpha_{QS}$. Translational deformation velocities in the rotational plane are further added to the variation in wind speed. The tangential and axial/perpendicular velocities are

(23) $$v_T(r,\Psi) = \Omega Rr + v_\infty\cos(\alpha_H)\sin(\Psi) + v_{i,T} = \left(r + \mu\sin(\Psi) + \lambda_{i,T}\right)\Omega R$$ $$v_P(r,\Psi) = v_\infty\sin(\alpha_H) + v_{i,P} = \left(\mu_z + \lambda_{i,P}\right)\Omega R$$

λ_i is the induced inflow ratio and μ_z is the helicopter advance ratio perpendicular to the rotor disk:

(24) $$\lambda_i = \frac{v_i}{\Omega R} \quad \text{and} \quad \mu_z = \frac{v_\infty\sin(\alpha_H)}{\Omega R}$$

With the assumption of a linear induced inflow, e.g., according to Drees [34], the inflow ratio is

$$\lambda_{i,T} = \frac{v_{i,T}}{\Omega R} = 0$$

(25) $$\lambda_{i,P} = \frac{v_{i,P}}{\Omega R} = \lambda_{0,P}\left(1 + k_x \frac{x}{R} + k_y \frac{y}{R}\right) = \lambda_{0,P}\left(1 + k_x r\cos\Psi + k_y r\sin\Psi\right)$$

With the longitudinal and lateral inflow gradients

(26) $$k_x = \frac{4}{3}(1 - \cos\mathrm{X} - 1.8\mu^2)\frac{1}{\sin\mathrm{X}}$$
$$k_y = -2\mu$$

The wake skew angle X is

(27) $$\mathrm{X} = \operatorname{atan}\left(\frac{\mu}{\mu_z + \lambda_{0,P}}\right)$$

$\lambda_{0,P}$ is the mean induced inflow velocity over the propeller disk and is

(28) $$\lambda_{0,P} = \frac{c_T}{2\sqrt{\mu^2 + \left(\mu_z + \lambda_{0,P}\right)^2}}$$

With $c_T = \frac{T}{\rho\pi R^2(\Omega R)^2}$

The initial steady-state simulation iteratively determines the thrust coefficient $c_T, \lambda_{0,P}$, and the thrust T. Inserting Eq. (25)-(28) into (23) yields

(29) $$\Phi(r,\Psi) = \operatorname{atan}\left(\frac{v_P}{v_T}\right) = \operatorname{atan}\left(\frac{\mu_z + \lambda_{0,P}\left(1 + k_x r\cos\Psi + k_y r\sin\Psi\right)}{r + \mu\sin(\Psi)}\right)$$

A Fourier transform of the oscillations of Φ shows negligible 2xP harmonics at the outboard section, as shown in Figure 8 for an exemplary lifting propeller. At the inboard section ($r = 0.35$), the 2xP and 3xP harmonic amplitudes are more pronounced, but the overall contribution of the section to aerodynamic loads is limited. Φ and $\dot{\Phi}$ in the frequency domain are

(30) $$\Phi(t) = \Phi_0 + \sum_{i=1}^{5} \underline{\hat{\Phi}}\, e^{j\,i\Omega t}$$
$$\dot{\Phi}(t) = \sum_{i=1}^{5} \underline{\hat{\dot{\Phi}}}\, e^{j\,i\Omega t} = \sum_{i=1}^{5} j\,i\Omega\, \underline{\hat{\Phi}}\, e^{j\,i\Omega t}$$

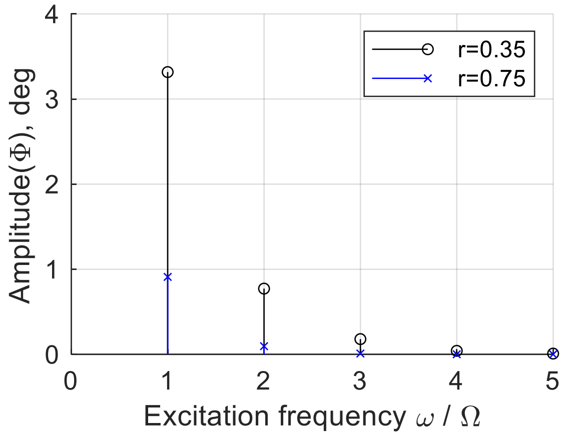

Figure 8: Amplitude spectrum of the wind angle $\mu = 0.15, \Omega = 209\frac{1}{s}, \alpha_H = 10°$

Note that in practical applications, lifting propellers are also excited at higher harmonics due to interference, e.g., with struts or the fuselage. Further, the linear inflow is only a crude approximation of the highly nonlinear inflow.

Wind Speed Variation Δw

At the outer sections ($r > 0.4$), the tangential velocity is significantly greater than the perpendicular velocity component. The wind speed w is

(31) $$w = \sqrt{\left(v_T + \dot{u}_y\right)^2 + (v_P + \dot{u}_z)^2} \approx v_T + \dot{u}_y = (r + \mu\sin(\Psi))\Omega R + \dot{u}_y = r\Omega R + \underline{\mu}\,\Omega R e^{j\Omega t} + \underline{\dot{u}}_y e^{j\,i\Omega t} = w_0 + \Delta w\, e^{j\,i\Omega t}$$

With

(32) $$w_0 = \Omega R r, \quad \underline{\mu}\, e^{j\Omega t} = \mu\, e^{j(-\frac{\pi}{2})} e^{j\Omega t}, \quad \text{and}$$
$$\dot{u}_y = \underline{\dot{u}}_y e^{j\,i\Omega t} = j\,i\Omega\, \underline{u}_y\, e^{j\,i\Omega t}$$

When excitation frequencies other than the rotational speed Ω are considered, only the deformation proportional term $\dot{u}_y$ is oscillating with the angular frequency $\omega = i\Omega$ $(i = 1,2,3 \ldots)$:

(33) $$\Delta w(\omega = i\Omega) = \underline{\dot{u}}_y\, e^{j\Omega t} \text{ for } i \geq 2$$

Summary of Aerodynamic Loads

The steady and dynamic parts of the aerodynamic loads are

$$\frac{dL}{dR} = \left(\frac{dL}{dR}\right)_{std} + \left(\frac{dL}{dR}\right)_{dyn} \approx$$

(34) $$\frac{\rho}{2} w_0^2\ c\ c_{l_0} + \frac{\partial(dL/dR)}{\partial w}\Delta w\ + \frac{\partial(dL/dR)}{\partial \alpha}\Delta\alpha =$$

$$\frac{\rho}{2} w_0\ c\ \left(w_0 c_{l0} + 2\ c_{l0}\ \Delta w + c_{l,\alpha}\ w_0\ \Delta\alpha\right)$$

Inserting Eq. (31) yields

(35) $$\frac{\partial(dL/dR)}{\partial w}\Delta w = \rho\ w_0\ c\ c_{l0}\big(\mu\Omega R sin(\Psi) + \dot{u}_y\big)$$

Using Eqs. (18)-(22) and (30) yields

(36) $$\frac{\partial(dL/dR)}{\partial \alpha}\Delta\alpha =$$

$$\frac{\rho}{2} w_0^2\ c\ c_{l,\alpha} \cdot \left(\alpha_{SD} + \left(\frac{\dot{h}}{w_0} + \frac{c}{2}\left(\frac{1}{2} - a\right)\frac{\dot{\alpha}}{w_0}\right) + \Phi\right) =$$

$$\frac{\rho}{2} w_0^2\ c\ c_{l,\alpha} \cdot \left(\alpha_{SD} + \frac{-\dot{u}_z \cos(\Phi_0) + \dot{u}_y \sin(\Phi_0) + \beta_0 \mu\Omega R}{w_0} + \frac{c}{2}\left(\frac{1}{2} - a\right)\frac{\dot{\alpha}_{SD} - \dot{\Phi}}{w_0} + \Phi\right)$$

The variation of aerodynamic moment is

(37) $$\left(\frac{dM_x}{dR}\right)_{dyn} = \frac{\rho}{2} w_0^2 c^2 c_{m_{0.25}} =$$

$$-\frac{\rho}{2} w_0 c^3 \frac{\pi}{8}\dot{\alpha} = -\frac{\rho}{2} w_0 c^3 \frac{\pi}{8}\left(\dot{\alpha}_{SD} - \dot{\Phi}\right)$$

With all non-steady deformations and deformation velocities being complex values.

4.4 Matrix Assembly

The dynamic loads can be further separated into functions of structural deformations, deformation velocities, and external excitations:

(38) $$\left(\frac{dL}{dR}\right)_{dyn} = f(\boldsymbol{u}) + f(\dot{\boldsymbol{u}}) + f_{external}$$

The deformation proportional loads are related as aerodynamic stiffness, i.e., they modify the structural stiffness matrix $\boldsymbol{K}$ by $\boldsymbol{K_{AE}}$

(39) $$\boldsymbol{K_{AE}}\ \boldsymbol{u} \sim -\frac{\rho}{2}\ w_0^2\ c\ c_{l,\alpha}\ \alpha_{SD}$$

Since the deformation and velocity related loads are considered on the left side of Eq. (9), the sign has to be inverted. The term proportional to deformation velocities modifies the damping matrix $\boldsymbol{C_R}$ by $\boldsymbol{C_{AE}}$

(40) $$\boldsymbol{C_{AE}}\ \dot{\boldsymbol{u}} \sim -\frac{\rho}{2} w_0 c \cdot \Big(\big(2c_{l0} + c_{l,\alpha}\sin(\Phi_0)\big)\ \dot{u}_y - c_{l,\alpha}\cos(\Phi_0)\,\dot{u}_z + c_{l,\alpha}\frac{c}{2}\left(\frac{1}{2} - a\right)\dot{\alpha}_{SD}\Big)$$

and $\boldsymbol{C_{AE}}\ \dot{\boldsymbol{u}} \sim \frac{\rho}{2} w_0 c^3 \frac{\pi}{8}\ \dot{\alpha}_{SD}$

The loads independent of unsteady structural deformations are the external dynamic loads due to the non-uniform inflow $\boldsymbol{F_{AE,NI}}$

(41) $$\boldsymbol{F_{AE,NI}} \sim \left(\frac{dL}{dR}\right)_{dyn_{ext}} = \frac{\rho}{2}\ w_0\ c \cdot \left(2c_{l0}\ \underline{\mu}\Omega R + c_{l,\alpha}\beta_0\mu\Omega R - c_{l,\alpha}\frac{c}{2}\left(\frac{1}{2} - a\right)\dot{\Phi} + w_0\ c_{l,\alpha}\ \Phi\right)$$

And the external moment

$$\left(\frac{dM_x}{dR}\right)_{dyn_{ext}} = \frac{\rho}{2} w_0 c^3 \frac{\pi}{8}\dot{\Phi}$$

The aerodynamic loads at the i[th] section have to be transformed to equivalent nodal loads to be processed within the FE method. In the structural (blade) coordinate system x_p, y_p, z_p, the distributed loads p are:

(42) $$p_{SD,y_i} = -\left(\frac{dL}{dR}\right)_{dyn_i} \cdot \sin\left(\Phi_{0_i}\right)$$

$$p_{SD,z_i} = +\left(\frac{dL}{dR}\right)_{dyn_i} \cdot \cos\left(\Phi_{0_i}\right)$$

$$m_{x_i} = \left(\frac{dM_x}{dR}\right)_{dyn_i}$$

The finite element procedure in the present approach uses cubic interpolation functions for bending deformation degrees of freedom and linear interpolation functions for torsional and longitudinal degrees of freedom. The interpolation functions are listed in appendix 7.1 The aerodynamic loads are determined at each aerodynamic section. Since the aerodynamic sections do not necessarily coincide with the structural nodes, the discrete sectional values are interpolated at each structural node using splines. Orthogonal projections transfer the loads from the quarter-chord line to the elastic axis. The torsional loads due to deviating shear centre and quarter chord point are considered within the projection of loads. The calculation of equivalent nodal loads due to external distributed sectional loads is straightforward and not described here.

Distributed loads p_i acc. Eq. (42) are assumed to vary linearly between two neighbouring structural nodes. The external work of equivalent nodal loads is

$$-\delta W_e = -\boldsymbol{F}\,\delta\boldsymbol{u} = \delta\boldsymbol{u}^T\boldsymbol{K_{AE}}\,\boldsymbol{u} =$$

(43)
$$\delta\boldsymbol{u}^T \int_{L_e} p(x)\,N(x)\,\boldsymbol{u}\,dx =$$

$$\delta\boldsymbol{u}^T \frac{L_e}{2} \int_{\xi=-1}^{+1} p(\xi)\,N(\xi)\,\boldsymbol{u}\,d\xi$$

The aerodynamic damping matrix can be derived similarly. The definition of both aerodynamic stiffness and damping matrix is in appendix 7.2.

5 RESULTS

5.1 Physical Interpretation

Dynamic Excitation Factor (DEF)

The Aq factor or the excitation factor EF are unsuited to quantify the magnitude of dynamic excitation of lifting propellers since they do not account for the varying wind speed. The external aerodynamic excitation is therefore quantified by a newly defined dynamic excitation factor DEF at 75% of the radius

$$\mathrm{DEF}_{75}(t) = \left(\frac{w}{w_0}\right)^2 \cdot \frac{c_l}{c_{l0}} - 1 \approx$$

(44)
$$\left(1 + \frac{4}{3}\mu\cos\left(\Omega t - \frac{\pi}{2}\right)\right)^2 \cdot \left(1 - \Phi\frac{c_{l,\alpha}}{c_{l0}}\cos\big(\Omega t + phase(\Phi)\big)\right) - 1$$

The dynamic excitation factor is a dimensionless measure to evaluate the external excitation with regard to the static loads. The DEF is defined to be zero in steady operation and unity if the external excitation is of the same magnitude as the steady loads. Figure 9 plots the oscillation of the DEF during one revolution.

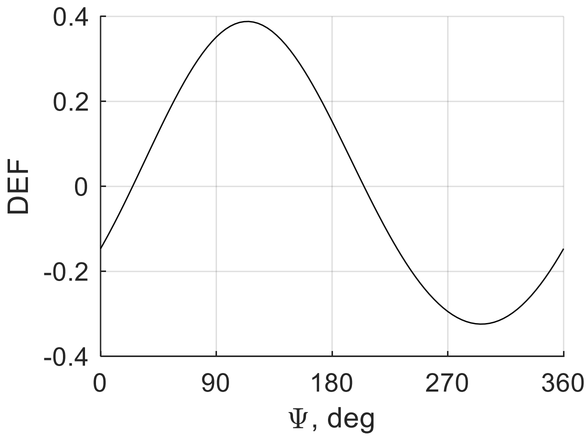

Figure 9: DEF75 oscillation during one revolution
$\mu = 0.105, \mu_z = 0.018, \lambda_{0,P} = 0.0135, \alpha_H = 10°$

The mean value is nonzero, and the oscillation includes minor 2xP contributions, as stated in section 4.3. The evaluation of the DEF is not required to determine the harmonic response but yields some physical insight. The dynamic excitation can be reduced by either

- reducing the advance ratio, i.e., increasing rotational speed or reducing horizontal flight speed
- Increasing c_{l0} or reducing $c_{l,\alpha}$

The wind angle Φ and its phase lag depend on the operational and geometrical parameters.

Dynamic Magnification

Depending on the damping ratio and the proximity to resonance frequencies, dynamic magnification significantly increases loads and deformations, as expressed by the transfer function in Figure 10. The first Eigenmode is typically above the 1xP excitation. The damping at resonance is dominated by the aerodynamic damping of the plunge motion. The amplification of loads occurs especially at the first Eigenmode. The second and third Eigenmode are less critical since both excitation and magnification are significantly lower compared to the first mode. The visualization of the transfer function yields information on the magnitude of amplification for a single rotational frequency. Since the rotational speed varies during flight, a Campbell plot further helps to compare excitation and resonance frequencies within the operational range.

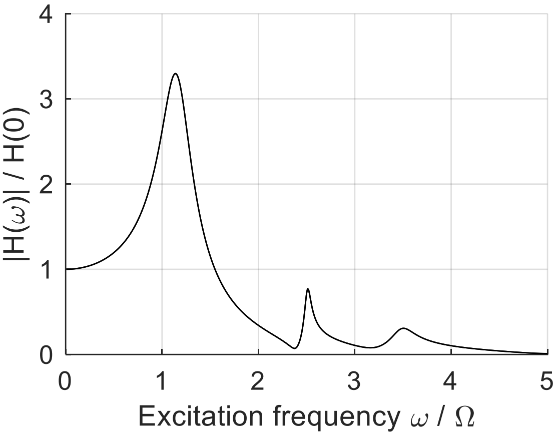

Figure 10: Transfer function of transverse load $\underline{F}_z$ and transverse deflection $\underline{u}_z$ at 75% radius

Dynamic magnification can be reduced by either increasing the blade's natural frequencies or by increasing aerodynamic damping.

5.2 Validation

Comparison to Transient Simulation

The structural deformations during forward flight of lifting propellers can be evaluated by calculating the harmonic response. Figure 11 compares the results of the harmonic response and a transient analysis. The deviations between both methods are approximately 10%.

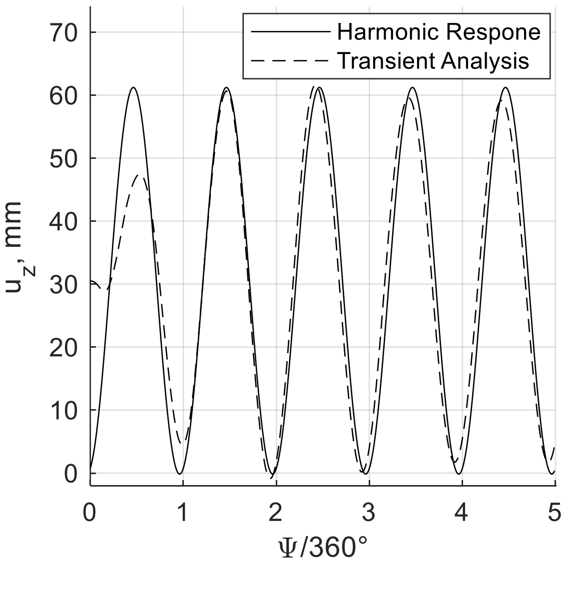

Figure 11: Comparison of transient and harmonic response analysis results of the tip node deformations

The harmonic deformations are added to the steady state deformations. Both simulations calculate quasi-steady aerodynamic loads. The transient simulation determines the lift coefficient based on actual polars for every specific Mach and Reynolds number instead of using linearized lift coefficients. Further, the transient simulation includes drag and moment variation based on polars, resulting in slight deviations in amplitude and phase lag. The deformation results of the transient simulation converge to a harmonic oscillation after 3-4 revolutions. The runtime of the transient simulation is approximately 30 seconds, while the harmonic response analysis requires 50ms, including the FFT of the inflow field and the matrix assembly on a single CPU core. The preprocessing of airfoil polars is not included in both values and requires additional 30 seconds at multiple CPU cores, but can be performed offline the optimization algorithm for common rotor airfoils. The amplitude of the simulation can also be approximated by the multiplication of the DEF and the dynamic magnification at 75% of the radius. Accordingly

$$u_z \approx \mathrm{DEF}_{75} \cdot \mathrm{H}(\Omega)_{75} \cdot u_{z,std} = 0.37 \cdot 2.6 \cdot u_{z,std} = 0.96 \cdot 31mm = 29.8mm \quad (45)$$

As mentioned above, the DEF and its use to approximate the deformations are not required for the harmonic response analysis. Still, it yields helpful physical insight.

Impact of Higher-Order Harmonics

It has been stated before that amplitude and dynamic magnification are most severe at the propeller rotational speed (1xP). Figure 12 compares the harmonic deformations during one revolution for the consideration of a single excitation frequency and a simulation considering the first five excitation frequencies. The deviations between both simulations are negligible, allowing to solely consider the 1xP loads for the present method. However, the linear inflow model and the quasi-steady aerodynamics inherently neglect primary sources of higher-order excitations. Further, blade and shaft loads might also include higher-order vibrations despite the deformation being dominated by oscillations within the rotational frequency. The authors want to highlight that accurate determination of higher-order vibratory loads demands more sophisticated models. Still, the novel method yields a rapid first-order approximation of dynamic propeller loads.

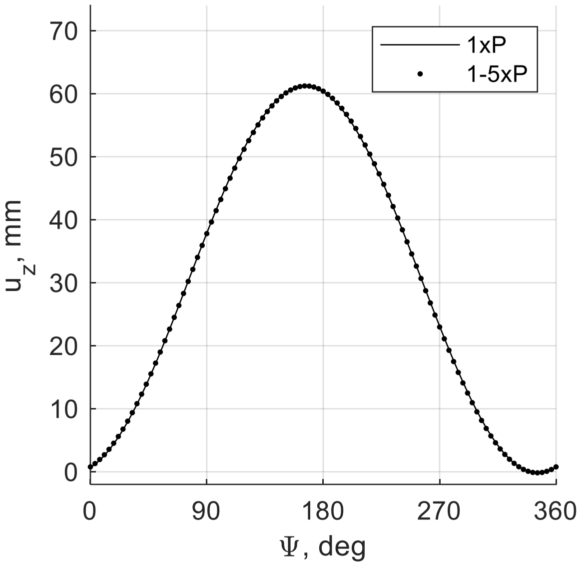

Figure 12: Comparison of harmonic response analysis including 1xP and 1-5xP results

For lifting propellers with two blades, already the 1xP dynamic bending loads are not filtered by the hub, resulting in significant shaft vibrations, see Ref. [24] for further explanation.

6 CONCLUSION

A novel approach to estimate dynamic blade loads of lifting propellers during forward flight has been presented. The conclusions are

- Aerodynamic loads and structural response show significant oscillations at the rotational frequency. Those so-called 1xP loads are especially important for two-bladed lifting propellers since 1xP loads are not filtered by the hub for two blades
- The impact of unsteady aerodynamic loads is limited. Still, the extension of the method to include Theodorsen's theory is feasible
- The dimensionless dynamic excitation factor DEF quantifies the external aerodynamic excitation occurring due to oblique inflow
- Significant dynamic magnification occurs if the blade's first resonance frequency is close to the rotational frequency
- While Campbell plots highlight the proximity of excitation and resonance frequencies, the transfer function of the presented method yields further information on the extent of dynamic magnification
- The approximation with the presented method in the frequency domain yields reasonable approximations compared to time-marching simulations
- High aspect ratio lifting propellers are susceptible to dynamic loads during forward flight due to low inherent stiffness and high lift curve slopes

Author contact

Felix Möhren, moehren@fh-aachen.de
Ole Bergmann, bergmann@fh-aachen.de
Frank Janser, janser@fh-aachen.de
Carsten Braun, c.braun@fh-aachen.de
Kai-Uwe Schröder,
kai-uwe.schroeder@sla.rwth-aachen.de

7 APPENDIX

7.1 Interpolation functions

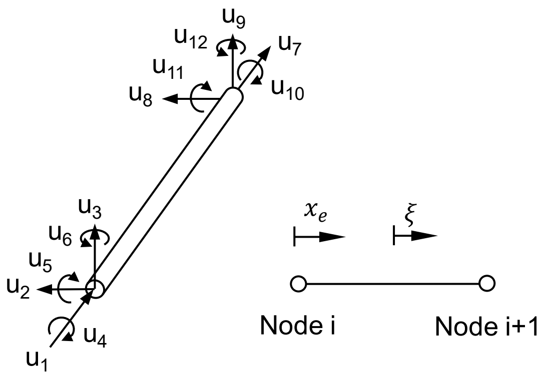

Figure 13: Finite Element degrees of freedom

$$u(\xi) = \begin{pmatrix} u_x \\ u_y \\ u_z \\ \theta_x \\ \theta_y \\ \theta_z \end{pmatrix} =$$

$$\begin{bmatrix} N_1 & 0 & 0 & 0 & 0 & 0 & N_2 & 0 & 0 & 0 & 0 & 0 \\ 0 & N_3 & 0 & 0 & 0 & N_4 & 0 & N_5 & 0 & 0 & 0 & N_6 \\ 0 & 0 & N_7 & 0 & N_8 & 0 & 0 & 0 & N_9 & 0 & N_{10} & 0 \\ 0 & 0 & 0 & N_{11} & 0 & 0 & 0 & 0 & 0 & N_{12} & 0 & 0 \\ 0 & 0 & N_{13} & 0 & N_{14} & 0 & 0 & 0 & N_{15} & 0 & N_{16} & 0 \\ 0 & N_{17} & 0 & 0 & 0 & N_{18} & 0 & N_{19} & 0 & 0 & 0 & N_{20} \end{bmatrix} \cdot \begin{pmatrix} u_1 \\ u_2 \\ u_3 \\ u_4 \\ u_5 \\ u_6 \\ u_7 \\ u_8 \\ u_9 \\ u_{10} \\ u_{11} \\ u_{12} \end{pmatrix}$$

With ξ as the dimensionless coordinate in the longitudinal direction $(-1 \leq \xi \leq +1)$, the form functions are:

$$N_1(\xi) = N_{11}(\xi) = \frac{1}{2}(1-\xi)$$
$$N_2(\xi) = N_{12}(\xi) = \frac{1}{2}(1+\xi)$$
$$N_3(\xi) = N_7(\xi) = \frac{1}{2}(1-\xi) - \frac{1}{4}\psi(\xi-\xi^3)$$
$$N_4(\xi) = -N_8(\xi) = \frac{L_e}{8}\{1-\xi^2-\psi(\xi-\xi^3)\}$$
$$N_5(\xi) = N_9(\xi) = \frac{1}{2}(1+\xi) + \frac{1}{4}\psi(\xi-\xi^3)$$
$$N_6(\xi) = -N_{10}(\xi) = -\frac{L_e}{8}\{1-\xi^2+\psi(\xi-\xi^3)\}$$

$$N_{13}(\xi) = -N_{17}(\xi) = \frac{3}{2L_e}\psi(1-\xi^2)$$
$$N_{14}(\xi) = N_{18}(\xi) = \frac{1}{2}(1-\xi) - \frac{3}{4}\psi(1-\xi^2)$$
$$N_{15}(\xi) = -N_{19}(\xi) = -\frac{3}{2L_e}\psi(1-\xi^2)$$
$$N_{16}(\xi) = N_{20}(\xi) = \frac{1}{2}(1+\xi) - \frac{3}{4}\psi(1-\xi^2)$$
$$\psi_y = \frac{1}{1+12\frac{EI_{zz}}{GA_{s_y}L_e^2}}, \qquad \psi_z = \frac{1}{1+12\frac{EI_{yy}}{GA_{s_z}L_e^2}}$$

with $GA_{s_{y/z}}$ as cross-sectional shear stiffness in the y- and z-direction, EI_{yy} and EI_{zz} as the bending stiffness in the y- and z-direction, and L_e as elemental length

ψ_y applies to the second and sixth row while ψ_z applies to the third and fifth row of the form function matrix.

7.2 Aerodynamic Influence Matrices

Aerodynamic Stiffness Matrix

The aerodynamic stiffness matrix is of size 12x12. All entries not defined below are zero:

$$K_{AE_{2,4}} = \sin(\Phi_{0_1})\frac{L_e}{2}\int N_{21}N_3 d\xi$$

$$K_{AE_{2,10}} = \sin(\Phi_{0_2})\frac{L_e}{2}\int N_{22}N_3 d\xi$$

$$K_{AE_{3,4}} = -\cos(\Phi_{0_1})\frac{L_e}{2}\int N_{21}N_7 d\xi$$

$$K_{AE_{3,10}} = -\cos(\Phi_{0_2})\frac{L_e}{2}\int N_{22}N_7 d\xi$$

$$K_{AE_{5,4}} = -\cos\left(\Phi_{0_1}\right)\frac{L_e}{2}\int N_{21}N_8 d\xi$$

$$K_{AE_{5,10}} = -\cos\left(\Phi_{0_2}\right)\frac{L_e}{2}\int N_{22}N_8 d\xi$$

$$K_{AE_{6,4}} = \sin(\Phi_{0_1})\frac{L_e}{2}\int N_{21}N_4 d\xi$$

$$K_{AE_{6,10}} = \sin\left(\Phi_{0_2}\right)\frac{L_e}{2}\int N_{22}N_4 d\xi$$

$$K_{AE_{8,4}} = \sin(\Phi_{0_1})\frac{L_e}{2}\int N_{21}N_5 d\xi$$

$$K_{AE_{8,10}} = \sin(\Phi_{0_2})\frac{L_e}{2}\int N_{22}N_5 d\xi$$

$$K_{AE_{9,4}} = -\cos(\Phi_{0_1})\frac{L_e}{2}\int N_{21}N_9 d\xi$$

$$K_{AE_{9,10}} = -\cos\left(\Phi_{0_2}\right)\frac{L_e}{2}\int N_{22}N_9 d\xi$$

$$K_{AE_{11,4}} = -\cos(\Phi_{0_1})\frac{L_e}{2}\int N_{21}N_{10} d\xi$$

$$K_{AE_{11,10}} = -\cos(\Phi_{0_2})\frac{L_e}{2}\int N_{22}N_{10} d\xi$$

$$K_{AE_{12,4}} = \sin(\Phi_{0_1})\frac{L_e}{2}\int N_{21}N_6 d\xi$$

$$K_{AE_{12,8}} = \sin(\Phi_{0_2})\frac{L_e}{2}\int N_{22}N_6 d\xi$$

With

$$N_{21}(\xi) = \frac{\frac{dL(\alpha)}{dR}}{\alpha}\cdot N_1(\xi) = -\frac{\rho}{2}w_{0_1}^2 c_1 c_{l_{\alpha 1}}\cdot\frac{1}{2}(1-\xi)$$

$$N_{22}(\xi) = \frac{\frac{dL(\alpha)}{dR}}{\alpha}\cdot N_2(\xi) = -\frac{\rho}{2}w_{0_2}^2 c_2 c_{l_{\alpha 2}}\cdot\frac{1}{2}(1+\xi)$$

Subscripts 1 and 2 denote parameters at the first and second node respectively of the considered element.

Aerodynamic Damping Matrix C_{AE}

All matrix entries not defined below are zero:

$$C_{AE_{2,2}} = \sin(\Phi_{0_1})\frac{L_e}{2}\int N_{23}N_3 d\xi$$

$$C_{AE_{2,3}} = \sin(\Phi_{0_1})\frac{L_e}{2}\int N_{24}N_3 d\xi$$

$$C_{AE_{2,4}} = \sin(\Phi_{0_1})\frac{L_e}{2}\int N_{25}N_3 d\xi$$

$$C_{AE_{2,8}} = \sin(\Phi_{0_2})\frac{L_e}{2}\int N_{26}N_3 d\xi$$

$$C_{AE_{2,9}} = \sin(\Phi_{0_2})\frac{L_e}{2}\int N_{27}N_3 d\xi$$

$$C_{AE_{2,10}} = \sin(\Phi_{0_2})\frac{L_e}{2}\int N_{28}N_3 d\xi$$

$$C_{AE_{3,2}} = -\cos(\Phi_{0_1})\frac{L_e}{2}\int N_{23}N_7 d\xi$$

$$C_{AE_{3,3}} = -\cos(\Phi_{0_1})\frac{L_e}{2}\int N_{24}N_7 d\xi$$

$$C_{AE_{3,4}} = -\cos(\Phi_{0_1})\frac{L_e}{2}\int N_{25}N_7 d\xi$$

$$C_{AE_{3,8}} = -\cos(\Phi_{0_2})\frac{L_e}{2}\int N_{26}N_7 d\xi$$

$$C_{AE_{3,9}} = -\cos(\Phi_{0_2})\frac{L_e}{2}\int N_{27}N_7 d\xi$$

$$C_{AE_{3,10}} = -\cos(\Phi_{0_2})\frac{L_e}{2}\int N_{28}N_7 d\xi$$

$$C_{AE_{4,4}} = \frac{L_e}{2}\int N_{29}N_{11} d\xi$$

$$C_{AE_{4,10}} = \frac{L_e}{2}\int N_{30}N_{11} d\xi$$

$$C_{AE_{10,4}} = \frac{L_e}{2}\int N_{29}N_{12} d\xi$$

$$C_{AE_{10,10}} = \frac{L_e}{2}\int N_{30}N_{12} d\xi$$

$$C_{AE_{5,2}} = -\cos(\Phi_{0_1})\frac{L_e}{2}\int N_{23}N_8 d\xi$$

$$C_{AE_{5,3}} = -\cos(\Phi_{0_1})\frac{L_e}{2}\int N_{24}N_8 d\xi$$

$$C_{AE_{5,4}} = -\cos(\Phi_{0_1})\frac{L_e}{2}\int N_{25}N_8 d\xi$$

$$C_{AE_{5,8}} = -\cos(\Phi_{0_2})\frac{L_e}{2}\int N_{26}N_8 d\xi$$

$$C_{AE_{5,9}} = -\cos(\Phi_{0_2})\frac{L_e}{2}\int N_{27}N_8 d\xi$$

$$C_{AE_{5,10}} = -\cos(\Phi_{0_2})\frac{L_e}{2}\int N_{28}N_8 d\xi$$

$$C_{AE_{6,2}} = \sin(\Phi_{0_1})\frac{L_e}{2}\int N_{23}N_4 d\xi$$

$$C_{AE_{6,3}} = \sin(\Phi_{0_1})\frac{L_e}{2}\int N_{24}N_4 d\xi$$

$$C_{AE_{6,4}} = \sin(\Phi_{0_1})\frac{L_e}{2}\int N_{25}N_4 d\xi$$

$$C_{AE_{6,8}} = \sin(\Phi_{0_2})\frac{L_e}{2}\int N_{26}N_4 d\xi$$

$$C_{AE_{6,9}} = \sin(\Phi_{0_2})\frac{L_e}{2}\int N_{27}N_4 d\xi$$

$$C_{AE_{6,10}} = \sin(\Phi_{0_2})\frac{L_e}{2}\int N_{28}N_4 d\xi$$

$$C_{AE_{8,2}} = \sin(\Phi_{0_1})\frac{L_e}{2}\int N_{23}N_5 d\xi$$

$$C_{AE_{8,3}} = \sin(\Phi_{0_1})\frac{L_e}{2}\int N_{24}N_5 d\xi$$

$$C_{AE_{8,4}} = \sin(\Phi_{0_1})\frac{L_e}{2}\int N_{25}N_5 d\xi$$

$$C_{AE_{8,8}} = \sin(\Phi_{0_2})\frac{L_e}{2}\int N_{26}N_5 d\xi$$

$$C_{AE_{8,9}} = \sin(\Phi_{0_2})\frac{L_e}{2}\int N_{27}N_5 d\xi$$

$$C_{AE_{8,10}} = \sin(\Phi_{0_2})\frac{L_e}{2}\int N_{28}N_5 d\xi$$

$$C_{AE_{9,2}} = -\cos(\Phi_{0_1})\frac{L_e}{2}\int N_{23}N_9 d\xi$$

$$C_{AE_{9,3}} = -\cos(\Phi_{0_1})\frac{L_e}{2}\int N_{24}N_9 d\xi$$

$$C_{AE_{9,4}} = -\cos(\Phi_{0_1})\frac{L_e}{2}\int N_{25}N_9 d\xi$$

$$C_{AE_{9,8}} = -\cos(\Phi_{0_2})\frac{L_e}{2}\int N_{26}N_9 d\xi$$

$$C_{AE_{9,9}} = -\cos(\Phi_{0_2})\frac{L_e}{2}\int N_{27}N_9 d\xi$$

$$C_{AE_{9,10}} = -\cos(\Phi_{0_2})\frac{L_e}{2}\int N_{28}N_9 d\xi$$

$$C_{AE_{11,2}} = -\cos(\Phi_{0_1})\frac{L_e}{2}\int N_{23}N_{10} d\xi$$

$$C_{AE_{11,3}} = -\cos(\Phi_{0_1})\frac{L_e}{2}\int N_{24}N_{10} d\xi$$

$$C_{AE_{11,4}} = -\cos(\Phi_{0_1})\frac{L_e}{2}\int N_{25}N_{10} d\xi$$

$$C_{AE_{11,8}} = -\cos(\Phi_{0_2})\frac{L_e}{2}\int N_{26}N_{10} d\xi$$

$$C_{AE_{11,9}} = -\cos(\Phi_{0_2})\frac{L_e}{2}\int N_{27}N_{10} d\xi$$

$$C_{AE_{11,10}} = -\cos(\Phi_{0_2})\frac{L_e}{2}\int N_{28}N_{10} d\xi$$

$$C_{AE_{12,2}} = \sin(\Phi_{0_1})\frac{L_e}{2}\int N_{23}N_6 d\xi$$

$$C_{AE_{12,3}} = \sin(\Phi_{0_1})\frac{L_e}{2}\int N_{24}N_6 d\xi$$

$$C_{AE_{12,4}} = \sin(\Phi_{0_1})\frac{L_e}{2}\int N_{25}N_6 d\xi$$

$$C_{AE_{12,8}} = \sin(\Phi_{0_2})\frac{L_e}{2}\int N_{26}N_6 d\xi$$

$$C_{AE_{12,9}} = \sin(\Phi_{0_2})\frac{L_e}{2}\int N_{27}N_6 d\xi$$

$$C_{AE_{12,10}} = \sin(\Phi_{0_2})\frac{L_e}{2}\int N_{28}N_6 d\xi$$

With

$$N_{23}(\xi) = \frac{\frac{dL(\dot{u}_y)}{dR}}{\dot{u}_y} \cdot N_1(\xi) = \frac{\rho}{2} w_{0_1} c_1 \left(2c_{l0_1} + c_{l,\alpha_1}\sin(\Phi_{0_1})\right) \cdot \frac{1}{2}(1-\xi)$$

$$N_{24}(\xi) = \frac{\frac{dL(\dot{u}_z)}{dR}}{\dot{u}_z} \cdot N_1(\xi) = \frac{\rho}{2} w_{0_1} c_1 \left(-c_{l,\alpha_1}\cos(\Phi_{0_1})\right) \cdot \frac{1}{2}(1-\xi)$$

$$N_{25}(\xi) = \frac{\frac{dL(\dot{\alpha})}{dR}}{\dot{\alpha}} \cdot N_1(\xi) = \frac{\rho}{2} w_{0_1} c_1 \left(c_{l,\alpha_1}\frac{c_1}{2}\left(\frac{1}{2} - a_1\right)\right) \cdot \frac{1}{2}(1-\xi)$$

$$N_{26}(\xi) = \frac{\frac{dL(\dot{u}_y)}{dR}}{\dot{u}_y} \cdot N_2(\xi) = \frac{\rho}{2} w_{0_2} c_2 \left(2c_{l0_2} + c_{l,\alpha_2}\sin(\Phi_{0_2})\right) \cdot \frac{1}{2}(1+\xi)$$

$$N_{27}(\xi) = \frac{\frac{dL(\dot{u}_z)}{dR}}{\dot{u}_z} \cdot N_2(\xi) = \frac{\rho}{2} w_{0_2} c_2 \left(-c_{l,\alpha_2}\cos(\Phi_{0_2})\right) \cdot \frac{1}{2}(1+\xi)$$

$$N_{28}(\xi) = \frac{\frac{dL(\dot{\alpha})}{dR}}{\dot{\alpha}} \cdot N_2(\xi) = \frac{\rho}{2} w_{0_2} c_2 \left(c_{l,\alpha_2}\frac{c_2}{2}\left(\frac{1}{2} - a_2\right)\right) \cdot \frac{1}{2}(1+\xi)$$

$$N_{29}(\xi) = \frac{dM_x(\alpha)}{dR}\frac{1}{\alpha}N_{11}(\xi) = \frac{\rho}{2} w_{0_1} c_1^3 \frac{\pi}{8} \cdot \frac{1}{2}(1-\xi)$$

$$N_{30}(\xi) = \frac{dM_x(\alpha)}{dR}\frac{1}{\alpha}N_{12}(\xi) = \frac{\rho}{2} w_{0_2} c_2^3 \frac{\pi}{8} \cdot \frac{1}{2}(1+\xi)$$

8 ACKNOWLEDGMENTS

The authors acknowledge the financial support by the Federal Ministry of Education and Research of Germany in the framework of IngenieurNachwuchs 2016 (project "DEFANA – Ducted Electric Fans for Novel Aircraft", project number 13FH638IX6).

9 REFERENCES

References

1. B. G. Marinus, M. Roger, R. A. van den Braembussche: Aeroacoustic and Aerodynamic Optimization of Aircraft Propeller Blades, Royal Military Academy; von Karman Institute for Fluid Dynamics; Ecole Centrale de Lyon (2010)
2. Sodja, J., Breuker, R., Nozak, D., Drazumeric, R., Marzocca P.: High- and Low-Fidelity Investigations of Flexible Propeller Blades. 52nd Aerospace Sciences Meeting (2014). https://doi.org/10.2514/6.2014-0410
3. Yamamoto, O., August, R.: Structural and aerodynamic analysis of a large-scale advanced propeller blade. Journal of Propulsion and Power **8**, 367–373 (1992)
4. van Zante, D.E.: Progress in open rotor research: A US perspective. In: Turbo Expo: Power for Land, Sea, and Air, V001T01A003 (2015)
5. Sodja, J., Drazumeric, R., Kosel, T., Marzocca P.: Design of Flexible Propellers with Optimized Load-Distribution Characteristics. Journal of Aircraft (2014). https://doi.org/10.2514/1.C032131
6. Marinus, B.: Multidisciplinary Optimization of Aircraft Propeller Blades. PhD thesis (2011)
7. Baert, L., Dumont, C., Beauthier, C., Sainvitu, C., Lepot, I., Blanchard, J.: Multidisciplinary Design of a Low-Noise Propeller: Part II—Efficient Aero-Acoustic-Mechanical Design Methodology Exploiting Surrogate Models in an Adaptive Design Space. In: Turbo Expo: Power for Land, Sea, and Air, V02DT38A023 (2020)
8. He, P., Koyuncuoglu, H., Hu, H., Dhulipalla, A., Hu, H., Hu, H.: High-fidelity aerodynamic and aerostructural optimization of UAV propellers using the adjoint method. In: AIAA SCITECH 2023 Forum AA 2023, p. 531
9. Vlastuin, J., Dejeu, C., Louet, A., Talbotec, J., Lepot, I., Lonfils, T., Leborgne, M.: Open rotor design strategy: from wind tunnel tests to full scale multi-disciplinary design. In: Turbo Expo: Power for Land, Sea, and Air, V02CT45A016 (2015)

10. Sullivan, J.P.: The Effect of Blade Sweep on Propeller Performance. AIAA 10th Fluid & Plasmadynamics Conference (1977). https://doi.org/10.2514/6.1977-716
11. Möhren, F., Bergmann, O., Janser, F., Braun, C.: On the influence of elasticity on propeller performance: a parametric study. CEAS Aeronautical Journal (2023). https://doi.org/10.1007/s13272-023-00649-y
12. Gur, O., Rosen, A.: Optimization of Propeller Based Propulsion System. Journal of Aircraft (2009). https://doi.org/10.2514/1.36055
13. EASA: CS-P Amendment 1, 1st edn.(P) (2006)
14. Yamane, T., Friedmann, P.P.: Aeroelastic tailoring analysis for preliminary design of advanced propellers with composite blades. Journal of Aircraft (1993). https://doi.org/10.2514/3.46315
15. Cornell, R.W., Rothman, E.A.: Structural design and analysis of prop-fan blades. AIAA/SAE/ASME 15th Joint propulsion conference (1979)
16. Kosmatka, J.B., Friedmann, P.P.: Vibration analysis of composite turbopropellers using a nonlinear beam-type finite-element approach. AIAA Journal (1989). https://doi.org/10.2514/3.10308
17. Braaten, M.E., Seeley, C., Tooley, M.: High Fidelity Fluid-Structure Interaction Analysis of a Wind Turbine Blade. In: 54th AIAA/ASME/ASCE/AHS/ASC Structures, p. 1693 (2013)
18. Ganguli, R., Chopra, I.: Aeroelastic optimization of a helicopter rotor with composite coupling. Journal of Aircraft **32**, 1326–1334 (1995)
19. Friedmann, P., Shanthakumaran, P.: Aeroelastic tailoring of rotor blades for vibration reduction in forward flight. In: 24th Structures, Structural Dynamics and Materials Conference, p. 916 (1983)
20. Friedmann, P.P.: Rotory-Wing Aeroelasticity - Current Status and Future Trends. AIAA Aerospace Sciences Meeting & Exhibit **39** (2001)
21. Friedmann, P.: Rotary-wing aeroelasticity with application to VTOL vehicles. AIAA 31st Structures, Structural Dynamics and Materials Conference, 1115 (1990)
22. Peters, D.A., He, C.J.: Correlation of measured induced velocities with a finite-state wake model. Journal of the American Helicopter Society **36**, 59–70 (1991)
23. Morillo, J.A., Peters, D.A.: Velocity field above a rotor disk by a new dynamic inflow model. Journal of Aircraft **39**, 731–738 (2002)
24. Amatt, W., Bates, W.E., Borst, H.V.: Summary of Propeller Design Procedures and Data. Volume II. Structural Analysis and Blade Design. USAAMRDL Technical Report 73-34B (1973)
25. Möhren, F., Bergmann, O., Janser, F., Braun, C.: On the Determination of Harmonic Propeller Loads. In: AIAA SCITECH 2023 Forum AA 2023, p. 2404
26. Billman, L.C., Gruska, C.J., Ladden, R.M., Leishman, D.K., Turnberg, J.E.: Large scale prop-fan structural design study. Volume 2: Preliminary design of SR-7 (1988)
27. Violette, J.A., Sullivan, W.E., Turnberg, J.E.: Large-Scale Advanced Prop-Fan (LAP) blade design (1984)
28. Chapman, D., Godston, J., Smith, D.: Testing of the 578-DX propfan propulsion system. In: 24th Joint Propulsion Conference, p. 2804 (1988)
29. Drela, M.: XFOIL: An Analysis and Design System for Low Reynolds Number Airfoils. In: Low Reynolds number aerodynamics, vol. 54. Springer (1989)
30. Betz, A., Prandtl, L.: Vier Abhandlungen zur Hydrodynamik und Aerodynamik, vol. 3. Universitätsverlag Göttingen, Göttingen (1919)
31. Bergmann, O., Götten, F., Braun, C., Janser, F.: Comparison and evaluation of blade element methods against RANS simulations and test data. In: CEAS Aeronautical Journal, vol. 13, 13th edn., pp. 535–557 (2022)
32. Johnson, W.: Helicopter Theory. Dover Publications, New York (1994)
33. van der Wall, B.G., Leishman, J.G.: On the influence of time-varying flow velocity on unsteady aerodynamics. j am helicopter soc **39**, 25–36 (1994)
34. Drees, J.M.: A theory of airflow through rotors and its application to some helicopter problems. Journal of the Helicopter Association of Great Britain, 79–104 (1949)